

Grain-by-Grain Compositional Variations and Interstitial Metals—A New Route toward Achieving High Performance in Half-Heusler Thermoelectrics

Sonia A. Barczak,[†] John E. Halpin,[‡] Jim Buckman,[§] Rodolphe Decourt,^{||,⊥} Michael Pollet,^{||,⊥} Ronald I. Smith,[#] Donald A. MacLaren,^{*,‡} and Jan-Willem G. Bos^{*,†}

[†]Institute of Chemical Sciences and Centre for Advanced Energy Storage and Recovery, School of Engineering and Physical Sciences, and [§]Institute of Petroleum Engineering, Heriot-Watt University, Edinburgh EH14 4AS, U.K.

[‡]SUPA, School of Physics and Astronomy, University of Glasgow, Glasgow G12 8QQ, U.K.

^{||}CNRS, ICMCB, UPR 9048, F-33600 Pessac, France

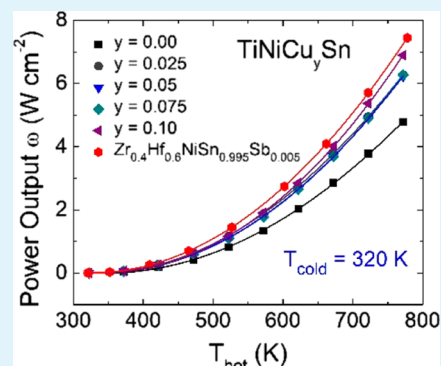
[⊥]University of Bordeaux, ICMCB, UPR 9048, F-33600 Pessac, France

[#]ISIS Facility, Rutherford Appleton Laboratory, Harwell Oxford, Didcot OX11 0QX, U.K.

Supporting Information

ABSTRACT: Half-Heusler alloys based on TiNiSn are promising thermoelectric materials characterized by large power factors and good mechanical and thermal stabilities, but they are limited by large thermal conductivities. A variety of strategies have been used to disrupt their thermal transport, including alloying with heavy, generally expensive, elements and nanostructuring, enabling figures of merit, $ZT \geq 1$ at elevated temperatures (>773 K). Here, we demonstrate an alternative strategy that is based around the partial segregation of excess Cu leading to grain-by-grain compositional variations, the formation of extruded Cu “wetting layers” between grains, and—most importantly—the presence of statistically distributed interstitials that reduce the thermal conductivity effectively through point-defect scattering. Our best TiNiCu_ySn ($y \leq 0.1$) compositions have a temperature-averaged $ZT_{\text{device}} = 0.3\text{--}0.4$ and estimated leg power outputs of $6\text{--}7$ W cm⁻² in the 323–773 K temperature range. This is a significant development as these materials were prepared using a straightforward processing method, do not contain any toxic, expensive, or scarce elements, and are therefore promising candidates for large-scale production.

KEYWORDS: thermoelectrics, structure–property relationships, half-Heusler, TiNiSn, phase segregation



1. INTRODUCTION

Thermoelectric (TE) generators directly convert waste heat into electricity and could become an important component of a sustainable energy future.¹ Large-scale application has so far been limited by their moderate efficiencies and relatively high cost, which derives from the scarcity of material resources.² Great progress has been made in improving the efficiency of thermoelectric materials over the past 2 decades, guided by several successful design strategies including the phonon-glass electron-crystal concept, band engineering, and nanostructuring.^{3–6} These have led to the design of many materials with peak ZT values above 1, which is generally seen as an indication of viability; in some cases, ZT can exceed 2.^{6,7} Here, $ZT = (S^2/\rho\kappa)T$ is the thermoelectric figure of merit, where S is the Seebeck coefficient, ρ is the electrical resistivity, κ is the sum of the lattice (κ_{lat}) and electronic (κ_{el}) thermal conductivities, and T is the absolute temperature. Another practical measure of performance is the power output, which is linked to the magnitude of the power factor (S^2/ρ), the dimensions of the legs, and the magnitude of κ .^{8,9}

Half-Heusler (HH) materials are highly promising for mid-temperature waste heat recovery because they balance the complex commercial trade-off between performance, cost, mechanical strength, and stability.¹⁰ The best n-type materials are based on XNiSn,^{11–14} while good p-type performance can be extracted from compositions based on XCoSb and X'FeSb (with $X = \text{Ti, Zr, and Hf}$ and $X' = \text{V and Nb}$).^{15–18} In terms of the individual thermoelectric parameters, the HH materials are characterized by large $S^2/\rho = 3\text{--}6$ mW m⁻¹ K⁻² and are, in effect, limited by their large κ_{lat} , which is typically $\kappa_{\text{lat}} = 3\text{--}4$ W m⁻¹ K⁻¹ for optimized compositions. This has stimulated several approaches to reduce κ_{lat} , including alloying at the X-site to increase point scattering of phonons, reduction of grain sizes to enhance boundary scattering of phonons, and segregation of full-Heusler (FH) XNi₂Sn phases in metal-rich XNi_{1+y}Sn compositions.^{19,20} The segregation of FH phases is of interest

Received: September 25, 2017

Accepted: January 9, 2018

Published: January 9, 2018

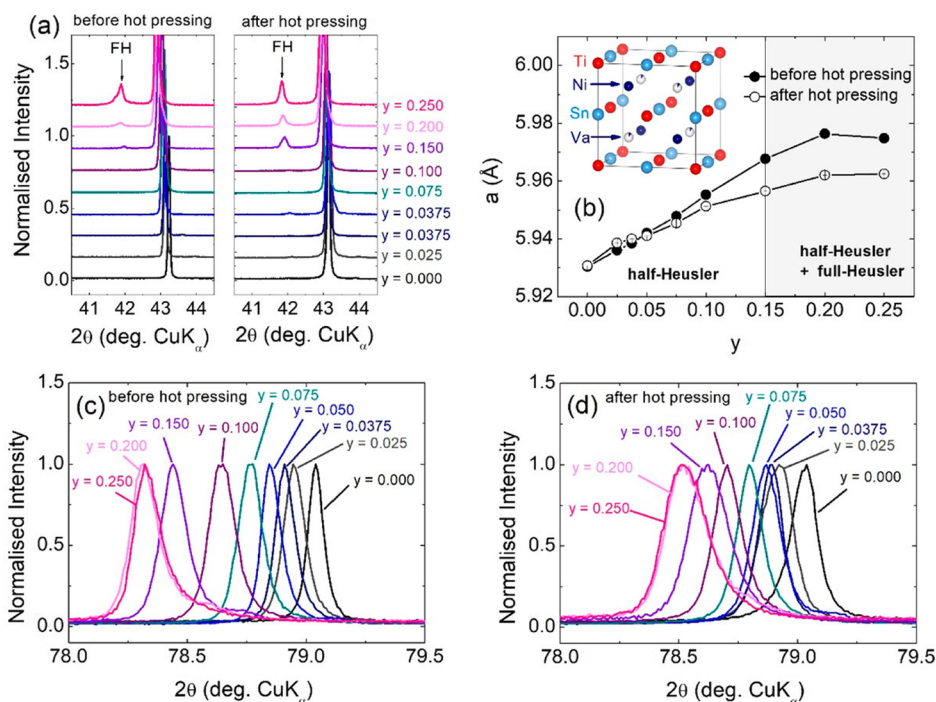


Figure 1. Comparison of the crystal structure before and after hot pressing: (a) close-up of the main HH and FH reflection in PXRD, (b) lattice parameters before and after hot pressing, and (c,d) close-up of the high-resolution (422) HH reflection before and after hot pressing, respectively. The inset in the panel (b) illustrates the HH structure, including the “vacant” tetrahedral site that is partially occupied in the TiNiCu_ySn samples.

because the similar crystal structure and lattice parameters of the HH and FH phases facilitate lattice coherence and thereby offer a means to effectively scatter phonons while maintaining charge carrier mobility.^{21,22} Theoretical studies point toward the instability of metal-rich $\text{XNi}_{1+y}\text{Sn}$ compositions with segregation into HH and FH phases being favored.^{23,24} Several experimental studies have used this instability to produce sub-10 nm FH inclusions^{21,22,25,26} that in some instances lead to carrier filtering and enhancement of the thermoelectric properties,^{21,22} but the formation of such inclusions is process-dependent, and other studies yield larger FH domains rather than obvious inclusions in the HH matrix.^{27–30} Developing a reliable, scalable production process for optimized nanostructuring remains problematic.

Here, we report on another manifestation of phase segregation that does not involve the formation of FH inclusions. The introduction of excess Cu to form the TiNiCu_ySn HH alloys instead produces relatively uniform HH structures on the nanoscale, where most of the excess metals randomly occupy interstitial sites and produce significant point scattering of phonons. Only small amounts of excess Cu ($y < 0.1$) are needed to achieve the optimal performance with power factors $S^2/\rho = 2\text{--}4 \text{ mW m}^{-1} \text{ K}^{-2}$ and low lattice thermal conductivities $\kappa_{\text{lat}} = 4\text{--}5 \text{ W m}^{-1} \text{ K}^{-1}$. Segregation is instead observed as grain-by-grain compositional variations, leading to the formation of a low fraction of grains with FH composition. Furthermore, extrusion of excess Cu from the HH matrix produces Cu-rich interfacial wetting layers between grains that appear to facilitate the formation of coherent grain boundaries. The best samples have a temperature-averaged $ZT_{\text{device}} = 0.3\text{--}0.4$ and calculated power outputs of $6\text{--}7 \text{ W cm}^{-2}$ from a $323\text{--}773 \text{ K}$ gradient. The latter are comparable to the leading HfNiSn -based compositions.^{11–13} These results are intriguing because they do not follow the prevailing trend to optimize HH systems toward boundary

scattering from inclusions but suggest the alternative strategy of employing interstitial point-defect scattering to be viable. Coupled with the use of inexpensive elements, this development could lead to commercially viable TE generator manufacture.

2. EXPERIMENTAL METHODS

2.1. Synthesis. TiNiCu_ySn ($0 \leq y \leq 0.25$) samples were prepared on a 3 g scale using standard solid-state methods. Stoichiometric amounts of elemental starting materials (Alfa Aesar; Ti, 325 mesh; Ni, 120 mesh; Cu, 625 mesh; and Sn, 100 mesh; all $\geq 99.8\%$ purity) were mixed together using a mortar and pestle and cold-pressed into 13 mm diameter pellets. The samples were wrapped in 0.025 mm thick Ta foil (Sigma-Aldrich) and initially annealed in evacuated quartz tubes at 900°C for 24 h. The mixtures were then reground to improve homogeneity, cold-pressed, wrapped in Ta foil, and annealed for a further 2 weeks at 900°C . In the first step, the heating rate was $10^\circ\text{C}/\text{min}$ and the cooling rate was $20^\circ\text{C}/\text{min}$. In the second step, the samples were inserted directly into the furnace at 900°C and air-quenched from 900°C . These samples are referred to as “before hot pressing”. In the final synthesis step, each composition was hot-pressed for 20 min at 875°C and 80 MPa using a homebuilt hot-press. These samples are referred to as “after hot pressing”. The densified Cu containing ingots were found to have $>98\%$ of the theoretical density, whereas the TiNiSn sample was 92% dense.

2.2. Structural Studies. Laboratory X-ray powder diffraction (PXRD) data were collected on a Bruker D8 ADVANCE diffractometer with $\text{Cu K}\alpha_1$ radiation. Long scans (8 h) suitable for Rietveld analysis were collected between $10 \leq 2\theta \leq 120^\circ$ and binned with a 0.01° step size. Neutron powder diffraction (NPD) data were collected on the Polaris instrument at the ISIS facility, Rutherford Appleton Laboratory, UK. Finely ground powders (1–2 g) were loaded into cylindrical V cans, and data were collected for 200–400 $\mu\text{A h}$ proton beam current to the ISIS target, corresponding to 1.5–3 h measurement time. The neutron scattering lengths are $b_{\text{Ti}} = -3.4 \text{ fm}$, $b_{\text{Ni}} = 10.3 \text{ fm}$, $b_{\text{Cu}} = 7.72 \text{ fm}$, and $b_{\text{Sn}} = 6.2 \text{ fm}$. Rietveld analysis was undertaken using the GSAS and EXPGUI programs.^{31,32} Scanning

electron microscopy and elemental mapping were done using a Quanta 650 FEG scanning electron microscope operated at 20 kV and equipped with an energy-dispersive X-ray spectroscopy (EDX) Oxford Instruments X-Max 150^N detector. Prior to analysis, the samples were polished using fine Al₂O₃ sandpaper down to 0.3 μm roughness. Transmission electron microscopy (TEM) and scanning TEM (STEM) were performed on a JEOL JEM-ARM200cF instrument equipped with a cold field-emission gun operating at 200 kV. Cross-sectional samples for TEM were milled directly from the hot-pressed pellets using an FEI Nova NanoLab focused ion beam system, yielding lamella that were typically 50–100 nm thick. These were then mounted onto Cu support grids that produced a weak Cu signal in EDX spectra because of secondary scattering; in contrast, the sample described in Figure S6 was mounted on an Al grid to avoid this problem so that the Cu content could be determined more accurately. STEM-EDX analysis was performed using a Bruker X-Flash detector, and background-subtracted K_α peaks were used for compositional analysis. The microscope is also equipped with a Gatan 965 Quantum ER spectrometer for electron energy loss spectroscopy (EELS). EELS elemental analysis was performed using the L_{2,3} edges of Ti, Ni, and Cu and the M_{4,5} edge of Sn. Spectra were deconvolved to remove plural scattering effects, background-subtracted, and analyzed using the cross-sectional data within DigitalMicrograph. The accuracy of absolute quantification of compositions using EELS is estimated to be of order 5%.

2.3. Thermoelectric Properties. The temperature dependence of S and ρ was measured using a Linseis LSR-3 instrument. The thermal conductivity (κ) was calculated from the measured thermal diffusivity (α), specific heat capacity (C_p), and density (d) using the relation $\kappa = \alpha C_p d$. The temperature dependence of α and C_p was measured using NETZSCH LFA 457 and PerkinElmer DSC 8500 instruments, respectively.

3. RESULTS

3.1. Crystal Structure from Diffraction. Structural information on the average structure of the TiNiCu _{y} Sn samples was obtained from PXRD and NPD, whereas the spatial distribution of the excess metals was investigated using STEM. The crystal structure of TiNiSn ($F\bar{4}3m$ space group; lattice parameter, $a \approx 5.95$ Å) consists of a face centered cubic Sn lattice with Ni occupying half the available tetrahedral sites and Ti in all octahedral sites (inset of Figure 1b). Filling the vacant tetrahedral sites fully results in the FH structure (e.g., TiNi₂Sn with $a \sim 6.1$ Å and a higher $Fm\bar{3}m$ space group symmetry).

The PXRD data show only HH reflections for $y \leq 0.10$, whereas both HH and FH peaks are present for larger y values (Figures 1a and S1). The samples of thermoelectric interest have $y \leq 0.10$ and therefore have all excess metals fully accommodated within the HH matrix. The HH lattice parameter was found to have decreased after the hot pressing that was used to consolidate the samples (Figure 1b). This is most pronounced for samples with $y \geq 0.15$ and reduces for samples with less Cu content. A comparison of the X-ray peak widths shown in Figure 1c,d reveals considerable broadening after hot pressing. Peak broadening is often attributed to a reduction in grain size, which is not observed by microscopy here. Instead, we attribute the peak broadening (and reduction in the lattice parameter) to the segregation of Cu. This leads to grain-by-grain compositional variations, with individual grains tending toward either HH or FH compositions. The kinetically arrested nature of the samples with varying amounts of excess Cu trapped in HH grains leads to the distribution of HH lattice parameters, and the observed diffraction peaks arise from an incoherent summation over all diffracting grains. By contrast, the FH reflections sharpen and increase in intensity (Figure 1a), signaling that the FH grains become more homogenous

and abundant during hot pressing. NPD was used to obtain information on the average composition of the HH phases. NPD is suited to this because of the good scattering contrast between Ti, Ni, Cu, and Sn. Rietveld analysis of the NPD data not only reveals the spontaneous presence of 2–3% of excess Ni in all samples but also indicates limits on the incorporation of Cu in the HH matrix. A summary of the fit results is presented in Tables S1 and S2, and the final fits are shown in Figures S2 and S3. For example, the fitted Cu content for $y = 0.05$ changes from 0.054(1) to 0.033(1), a 20% reduction upon hot pressing. Similar reductions were observed for the other samples. The STEM analysis below reveals that the excess Cu is extruded from HH grains with individual grains tending toward either a HH or FH composition. Large area SEM-EDX elemental maps confirm the overall unchanged compositions of the samples after hot pressing (Figure S4).

3.2. Microstructure Analysis. A typical STEM image of a thin lamella selected from the center of the $y = 0.25$ hot-pressed sample is presented in Figure 2a. We choose this sample for discussion because the higher Cu content is easier to map, but similar structural features are observed for other samples and an analysis of the $y = 0.1$ sample is presented in the Supporting Information (Figures S5 and S6).

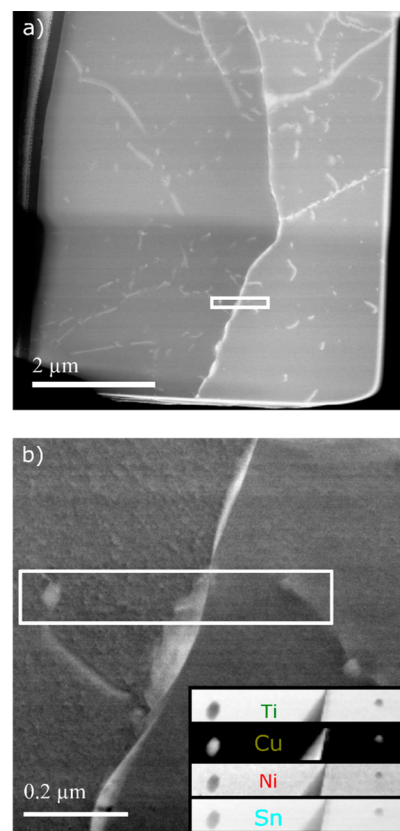


Figure 2. Analysis of the microstructure after hot pressing. STEM analysis of a hot-pressed $y = 0.25$ sample. (a) In dark-field STEM, grain boundaries and strain-inducing defects appear bright. The lamella has been selected from the center of the as-prepared sample and thinned using focused ion beam techniques (the material to the lower half of the image has been thinned further than that above). (b) Elemental analysis, by EELS, across a typical grain boundary and spot-features with (inset) maps of the distribution Ti, Cu, Ni, and Sn within the indicated region. Both the boundary and the spots are copper-rich. The approximate location of image (b) is indicated in image (a).

Contrast in the dark-field image of Figure 2a derives principally from thickness variations and strain due to the presence of crystallographic defects, including grain boundaries and dislocations. The image clearly reveals the boundaries between grains that are typically several microns in diameter. There is no evidence of voids between grains, consistent with full densification. Also visible is a relatively small number of white streaks and spots, some of which are analyzed further in Figure 2b. The inset in Figure 2b shows the EELS signals which reveals that both the grain boundary (running vertically through the middle of the inset panels) and the occasional brighter spots are Cu-rich, although we stress that these spots are at too low a density to account for a significant fraction of the Cu. High-resolution TEM imaging (not shown) suggests the arcs linking these spots to the boundary to be dislocations and it is tempting to interpret these as providing a low-energy diffusion pathway to facilitate Cu extrusion during hot pressing. The relative intensities of Ti, Ni, and Sn on either side of the grain boundary are similar, and we conclude that the grains are both of HH composition, with the Cu content around $\sim 2\%$, the estimated EELS detectability limit in this case. An important conclusion from the TEM analysis is that we do not find evidence for nanoscale FH inclusions, apart from these infrequent Cu-rich spots. There is no obvious splitting of diffraction spots from within an individual grain, or contrast variations in TEM or STEM, that would suggest nanoscale HH–FH segregation. Instead, elemental mapping indicates that individual micron-sized grains have a relatively uniform composition but can differ from their neighbors, producing what we term here as grain-by-grain compositional variations and the formation of Cu-rich grain boundaries. One such grain boundary is presented in Figure 3a, where the boundary runs vertically across the center of the image. The sample is oriented to view the grain in the left half of the image along a (111) direction, consistent with the indexed spots in the selected area electron diffraction pattern (inset). The material in the right half of the image is aligned along a (1n0)-type direction, contributing the circled spots to the diffraction pattern. The grain boundary itself appears (in projection) to be of order 2 nm wide but is coherent, with the lattice lines in the two grains meeting at 135° and without obvious dislocations within the field of view.

EELS elemental analysis of a much wider region across the same boundary is presented in Figure 3b,c, which suggests compositions of $\text{Ti}_{1.0}\text{Ni}_{1.04}\text{Sn}_{1.09}$ in the right grain and $\text{Ti}_{1.0}\text{Ni}_{1.22}\text{Cu}_{0.33}\text{Sn}_{1.02}$ in the left grain (again noting the estimated 2% detectability limit for EELS). There is no obvious texture in the elemental maps on either side of the grain boundary, suggesting a very uniform composition within each grain. A similar analysis of a grain boundary for the $y = 0.1$ sample is presented in Figure S6. In this case, EDX was used and more accurate compositions were obtained. An almost identical boundary structure was observed with approximate compositions on the either side of $\text{Ti}_{1.0}\text{Ni}_{1.09}\text{Cu}_{0.09}\text{Sn}_{1.04}$ and $\text{Ti}_{1.0}\text{Ni}_{0.99}\text{Cu}_{0.04}\text{Sn}_{1.02}$, again demonstrating the tendency of the excess metals to segregate into grains with FH compositions. As observed in Figures 2 and 3, the grain boundary is Cu-rich, indicating the formation of a Cu “wetting layer” that high-resolution imaging suggests is coherent with the surrounding lattices.

The main conclusion from the TEM is therefore that the composition of individual grains differs with segregation of excess metals (Ni and Cu) toward a small number of FH grains.

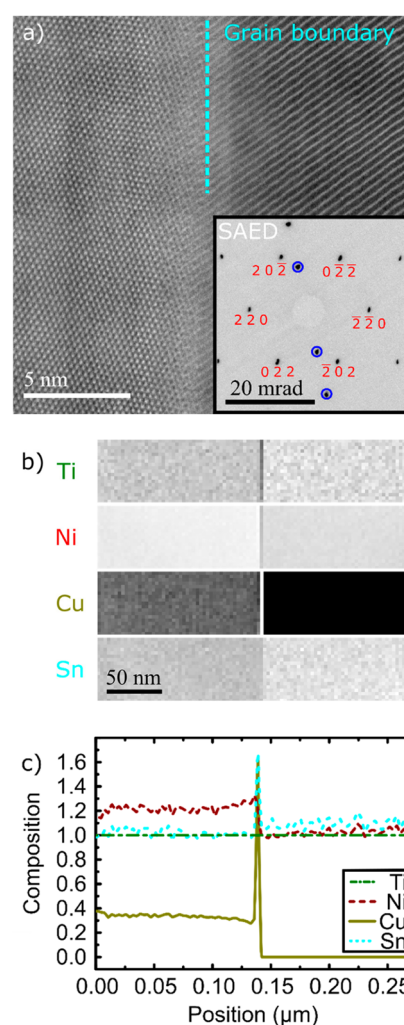


Figure 3. Evaluation of a grain boundary. (a) High-resolution STEM image with (inset) selected area diffraction of a boundary between a Cu-rich (left) and a Cu-deficient grain (right). Diffraction spots from the lower grain are circled. The two lattices meet coherently. (b) EELS analysis across the boundary indicates uniform composition within each of the grains and a clear Cu enrichment at the boundary. (c) Approximate composition of the two regions is $\text{Ti}_{1.0}\text{Ni}_{1.04}\text{Sn}_{1.09}$ in the right region and $\text{Ti}_{1.0}\text{Ni}_{1.22}\text{Cu}_{0.33}\text{Sn}_{1.02}$ in the left region.

There is no evidence of nanoscale-texturing of the Cu content to form an appreciable number of nanoscale Cu inclusions that would affect the bulk thermal transport.

3.3. Thermoelectric Properties. The temperature dependence of the electrical resistivity ρ , Seebeck coefficient S , and power factor S^2/ρ is shown in Figure 4. All samples are n-type semiconductors, as indicated by the negative values of $S(T)$. The magnitudes of both $S(T)$ and $\rho(T)$ decrease sequentially with increasing Cu content (Figure 4a,b), and there is a clear change in their temperature-dependent trends upon even low Cu doping. The TiNiSn sample is a non-degenerate semiconductor with decreasing $\rho(T)$. Introduction of excess Cu results in a transition to a metallic $\rho(T)$, indicative of high levels of doping and degenerate semiconducting behavior. Efficient n-type doping is confirmed by Hall measurements, which show an order of magnitude increase in the carrier concentration between $y = 0$ and $y = 0.075$ without degradation of the carrier mobility (from $n = 1.03 \times 10^{20} \text{ cm}^{-3}$ to $n = 1.46 \times 10^{21} \text{ cm}^{-3}$, respectively—see Table S3). As a

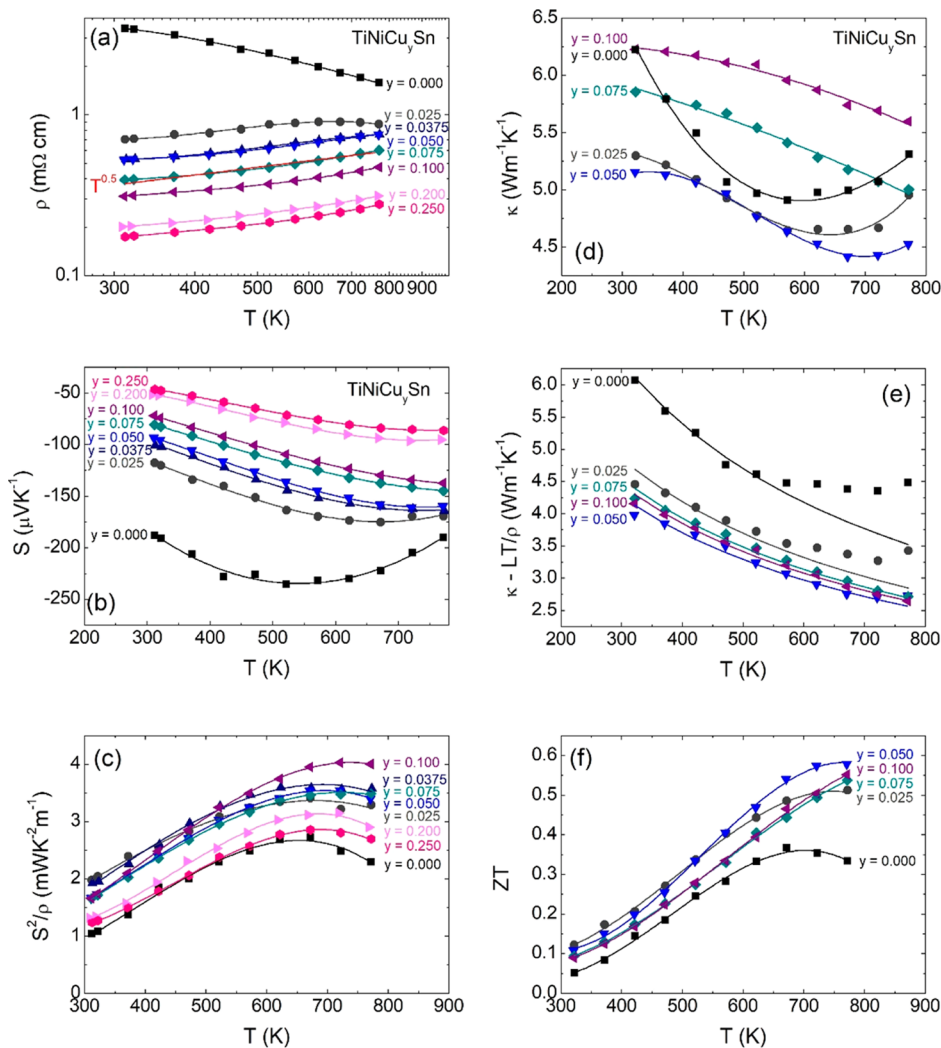


Figure 4. TE properties: temperature dependence of (a) electrical resistivity, ρ , (b) Seebeck coefficient, S , (c) thermoelectric power factor, S^2/ρ , (d) total thermal conductivity, κ , (e) thermal conductivity with the Wiedemann–Franz electronic component subtracted, $\kappa - LT/\rho$, and (f) figure of merit, ZT , for the TiNiCu_ySn samples.

result, $\rho_{300\text{K}}$ decreases by a factor of eight, from 3.4 $\text{m}\Omega\text{ cm}$ (for $y = 0$) to 0.4 $\text{m}\Omega\text{ cm}$ (for $y = 0.075$).

In the degenerate limit, conductivity is expected to follow an inverse power law with temperature, that is, $\rho \approx T^z$ and carriers are usually scattered by acoustic phonons for a homogenous matrix without disorder, for which $z = 3/2$. Using the exponent z to determine the dominant carrier scattering mechanism, a log–log plot of $\rho(T)$ yields $z = 0.5$ for our samples with $y \geq 0.025$ (Figure 4a), which is consistent with the presence of interstitial metals.³³ The resulting S^2/ρ is greatly increased and attains maximum values of $\sim 2\text{ mW m}^{-1}\text{ K}^{-2}$ at 323 K and $\sim 4\text{ mW m}^{-1}\text{ K}^{-2}$ at 700 K for $0.05 \leq y \leq 0.1$ (Figure 4c). The 323 K and 700 K peak values are ~ 100 and $\sim 60\%$ improved, respectively, compared to TiNiSn . Increasing y above 0.1 results in the reduction of the measured S^2/ρ , which correlates with the observation of distinct metallic FH phases in PXRD and NPD.

The $\kappa_{\text{total}}(T)$ for the $0 \leq y \leq 0.1$ compositions was calculated from experimental heat capacity and thermal diffusivity data (Figure S7) and is shown in Figure 4d. The $y = 0$ sample shows a clear increase in $\kappa(T)$ above 550 K because of the onset of minority conduction, but the trend is gradually suppressed as y increases and is not evident for $y \geq 0.075$. At 323 K, $\kappa_{\text{total}} = 6.2$

$\text{W m}^{-1}\text{ K}^{-1}$ for $y = 0$, which decreases to $\kappa_{\text{total}} = 5.2\text{ W m}^{-1}\text{ K}^{-1}$ for $y = 0.05$ and then increases to a similar $\kappa_{\text{total}} = 6.2\text{ W m}^{-1}\text{ K}^{-1}$ for $y = 0.1$. The increase for $y > 0.05$ is caused by the metallic nature of the samples and the rapid increase in $\kappa_{\text{el}} = LT/\rho$, where L is the Lorenz number. The transition to degenerate conducting behavior that is evident in $\rho(T)$ and $S(T)$ suggests a single dominant carrier type. On the basis of this observation, $S(T)$ was evaluated using the single parabolic band (SPB) model in the degenerate limit.³⁴ The result of this analysis is shown in Figure S8a and results in an overestimate of $S(T)$ at higher temperatures. This suggests either that multiple bands contribute to the electronic transport or that the bands are nonparabolic, such as, for example, the Kane model applied to ZrNiSn -based HH materials.³⁵ To obtain a reliable estimate of the Lorenz number, the empirical expression in ref 36 was used. This is estimated to be within 20% accuracy for thermoelectric materials with non-SPB carrier transport. The calculated $L(T)$ and $\kappa_{\text{el}}(T)$ values are given in Figure S8b,c. The extracted $\kappa_{\text{total}}(T) - LT/\rho$ values are shown in Figure 4e. These values correspond to κ_{lat} below the onset of bipolar thermal transport, which is $\sim 550\text{ K}$ for $y = 0$, increasing to $\sim 700\text{ K}$ for $y = 0.05$ and above the upper limit of the measurement for $y \geq 0.075$. This reveals a substantial reduction from $6.0\text{ W m}^{-1}\text{ K}^{-1}$

($y = 0$) to $4.5 \text{ W m}^{-1} \text{ K}^{-1}$ ($y = 0.025$) at 323 K, while similar values are observed for larger y values. The observed $\kappa_{\text{lat},323\text{K}} = 6 \text{ W m}^{-1} \text{ K}^{-1}$ for TiNiSn is much smaller than the expected values with $\kappa_{\text{lat},323\text{K}} = 10\text{--}15 \text{ W m}^{-1} \text{ K}^{-1}$ for the XNiSn ($X = \text{Ti, Zr, and Hf}$) parent materials.^{37,38}

Calculations of the phonon mean free path (MFP) for HH materials suggest that 90% of the thermal transport occurs by phonons with a MFP $< 1 \mu\text{m}$.³⁹ TEM reveals the presence of large relatively uniform grains of $2\text{--}5 \mu\text{m}$ dimensions, indicating that the main reduction in κ_{lat} must be caused by the interstitial metals within the HH grains. The results of the Callaway fits are given in Table 1, and the final fits are shown in

Table 1. Thermal Conductivity Modeling: Callaway Fit Parameters for the TiNiCu_ySn Samples^a

composition	4d-site occupancy	$\kappa_{323\text{K-LT}/\rho}$ ($\text{W m}^{-1} \text{ K}^{-1}$)	Γ	Γ_{exp}
TiNiSn	Ni _{0.030}	6.0	0.07	0.06
TiNiCu _{0.025} Sn	Ni _{0.03} Cu _{0.018} ^b	4.5	0.11	0.12
TiNiCu _{0.05} Sn	Ni _{0.03} Cu _{0.033}	4.0	0.14	0.16
TiNiCu _{0.075} Sn	Ni _{0.03} Cu _{0.053} ^b	4.2	0.17	0.14
TiNiCu _{0.1} Sn	Ni _{0.03} Cu _{0.073}	4.2	0.21	0.15

^aThe 4d-site occupancy was taken from Rietveld fits to the NPD data (see Table S2). Γ and Γ_{exp} are the calculated and experimental point-defect scattering parameters, respectively. ^bFor all fits: $B = 5 \mu\text{m}$ and $B_{\text{U}} = 2.1 \times 10^{-18} \text{ s K}^{-1}$.

Figure 4e. In these fits, the phonon–phonon scattering strength (B_{U}) was kept the same for all samples and the boundary scattering parameter was fixed at $B = 5 \mu\text{m}$.

The experimental point-defect scattering strength $\Gamma_{\text{exp}} = 0.06$ for $y = 0$, increasing to $\Gamma_{\text{exp}} = 0.15(1)$ for $0.05 \leq y \leq 0.10$, which have identical κ_{lat} . The calculated point-defect scattering strengths, Γ , are found to be in good agreement on the

assumption that the interstitials form bonds and that these enhance the phonon scattering beyond that expected based on simple mass effects. Full details of the Callaway analysis are given in the Supporting Information.

The temperature dependence of the figure of merit, ZT is shown in Figure 4f. For $y = 0$, $ZT = 0.05$ at 323 K and increases to $ZT = 0.35$ at 673 K. The increase in S^2/ρ and reduction of κ_{lat} due to the introduction of excess Cu lead to $ZT \approx 0.1$ at 323 K ($0.025 \leq y \leq 0.1$), while the peak ZT s = $0.5\text{--}0.6$ are observed at $650\text{--}773 \text{ K}$. The reduction in κ_{lat} upon the introduction of excess Cu is partially offset by the increased electronic contribution (LT/ρ), thereby limiting the ZT values. Nevertheless, the reported ZT values represent a 100% improvement over TiNiSn near room temperature and a $\sim 50\%$ improvement in terms of peaks ZT .

3.4. Efficiency and Power Output. The efficiency and the power output are important considerations for application of a material in a TE device. The efficiency (η) of a TE material is given by⁹

$$\eta = \frac{T_{\text{h}} - T_{\text{c}}}{T_{\text{h}}} \frac{\sqrt{1 + ZT_{\text{device}}} - 1}{\sqrt{1 + ZT_{\text{device}} + \frac{T_{\text{c}}}{T_{\text{h}}}}} \quad (1)$$

Here, ZT_{device} is the average of ZT over the temperature gradient being exploited, T_{h} is the hot-side temperature, and T_{c} is the cold-side temperature. The power output of a thermoelectric material can be estimated using⁸

$$\omega = \frac{\text{PF}_{\text{device}}(\Delta T)^2/2h}{\left(1 + \frac{\text{PF}_{\text{device}}T_{\text{hot}}}{2\kappa_{\text{device}}}\right) + \sqrt{1 + \text{PF}_{\text{device}}\bar{T}/\kappa_{\text{device}}}} \quad (2)$$

Here, $\text{PF}_{\text{device}}$ and κ_{device} are the averages of S^2/ρ and κ over the exploited temperature gradient, respectively, h is the length of the thermoelectric leg, $\Delta T = T_{\text{h}} - T_{\text{c}}$, and \bar{T} is the average

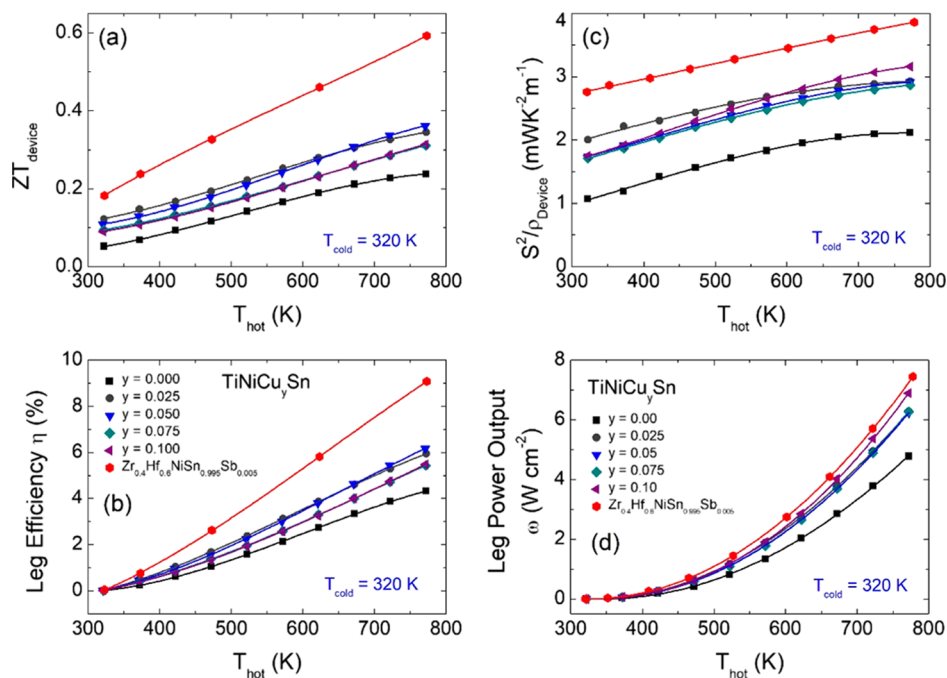


Figure 5. Leg efficiencies and power outputs: temperature dependence of (a) ZT_{device} , (b) the efficiency, (c) $\text{PF}_{\text{device}}$, and (d) the power output for the TiNiCu_ySn samples as a function of hot-side temperature. The data for the $\text{Zr}_{0.4}\text{Hf}_{0.6}\text{NiSn}_{0.995}\text{Sb}_{0.005}$ sample is representative of the best samples in the literature and was taken from ref 13.

temperature. The temperature dependence of ZT_{device} , PF_{device} , the leg efficiencies, and leg power outputs are shown in Figure 5. This reveals that $ZT_{\text{device}} = 0.25$ and the leg efficiency is 4% from a 450 K gradient for TiNiSn with $T_c = 320$ K. For the samples with excess Cu, the performance improves to $ZT_{\text{device}} = 0.3$ – 0.4 and $\sim 6\%$ conversion efficiency from the same temperature gradient (Figure 5a,b).

The PF_{device} increases by 50% from $2 \text{ mW m}^{-1} \text{ K}^{-2}$ from a 450 K gradient for TiNiSn to $\sim 3 \text{ mW m}^{-1} \text{ K}^{-2}$ for the excess Cu samples (Figure 5c). This enables an improved leg power output, increasing from 5 W cm^{-2} ($y = 0$) to 7 W cm^{-2} ($y = 0.1$) with a 450 K gradient and using $h = 2 \text{ mm}$ (Figure 5d). For comparison, the ZT_{device} , leg efficiency, PF_{device} , and leg power output for a representative state-of-the-art $\text{Zr}_{0.4}\text{Hf}_{0.6}\text{NiSn}_{0.995}\text{Sb}_{0.005}$ alloy are also shown in Figure 5.^{11–13} This reveals that the TiNiCu_ySn materials are competitive with the best HH materials in terms of power output ($\omega \approx 7 \text{ W cm}^{-2}$) but are characterized by a lower efficiency (6 vs 9%) because of the competing requirements for efficiency and power output. The former is linked to having a high ZT_{device} for which a low $\kappa(T)$ is essential, while the power output relies on having a large PF_{device} but also on the magnitude of $\kappa(T)$ because of the coupled nature of the flow of heat and charge.⁸ This illustrates that other performance indicators, such as power output, should be considered along with ZT in judging the suitability of a thermoelectric material. We tested the thermoelectric properties under repeated cycling and did not observe any changes, which is critical for the construction of viable devices. Furthermore, a test where a large current density was forced through a TiNiCu_{0.1}Sn sample at room temperature did not produce any changes in the sample composition (e.g., migration of Cu to the surface).

4. CONCLUSIONS

Significant improvements in S^2/ρ and reductions in κ_{lat} near room temperature have been achieved in TiNiCu_ySn HH alloys. These samples are characterized grain-by-grain compositional variations with a tendency toward the formation of either HH or FH compositions. No evidence for nanoscale FH inclusions is observed, and the grains contain randomly distributed excess metals instead. Some Cu segregation occurs at grain boundaries and this leads to the formation of “wetting layers”, enabling full densification and facile electronic transport. The observed segregation agrees with the widely reported thermodynamic instability of metal-rich HH compositions. Pisarenko analysis (Figure S9) indicates an increase in the effective carrier mass from $\sim 3m_e$ ($y = 0$) to $\sim 5m_e$ ($y = 0.075$), which suggests a substantial modification of the electronic band structure. This is in keeping with the strong impact of the interstitials on the thermal transport. The improvements in the individual thermoelectric parameters enable viable efficiencies and leg power outputs. Our results are particularly significant as these HH materials do not contain any toxic or expensive elements (such as Hf) and are produced using a simple processing route. These materials are therefore promising candidates for large-scale production. The present results demonstrate a new route to control the nanostructure of HH alloys through phase segregation, which should transfer to other HH material systems under investigation for thermoelectric waste heat recovery.

■ ASSOCIATED CONTENT

Supporting Information

The Supporting Information is available free of charge on the ACS Publications website at DOI: 10.1021/acsami.7b14525.

Tables with crystallographic information and Hall data; PXRD patterns for all TiNiCu_ySn samples; Rietveld fits to NPD data on selected TiNiCu_ySn samples before and after hot pressing; SEM and EDX elemental maps; additional TEM data on the $y = 0.1$ and $y = 0.25$ samples; and thermal diffusivity, heat capacity, Pisarenko plot, SPB analysis, Lorenz number and electronic thermal conductivity for the TiNiCu_ySn samples (PDF)

■ AUTHOR INFORMATION

Corresponding Authors

*E-mail: j.w.g.bos@hw.ac.uk.

*E-mail: dmaclaren@physics.org.

ORCID

Jan-Willem G. Bos: 0000-0003-3947-2024

Notes

The authors declare no competing financial interest.

Raw data underpinning this report are available at <http://dx.doi.org/10.5525/gla.researchdata.572>.

■ ACKNOWLEDGMENTS

The EPSRC is acknowledged for funding the work on nanostructured half-Heuslers for thermoelectric waste heat recovery (grants EP/N01717X/1 and EP/N017218/1) and a studentship for S.A.B. The STFC is acknowledged for provision of beam time at the ISIS facility (award RB1520223).

■ REFERENCES

- (1) Snyder, G. J.; Toberer, E. S. Complex thermoelectric materials. *Nat. Mater.* **2008**, *7*, 105–114.
- (2) Yee, S. K.; LeBlanc, S.; Goodson, K. E.; Dames, C. \$ per W metrics for thermoelectric power generation: beyond ZT. *Energy Environ. Sci.* **2013**, *6*, 2561–2571.
- (3) Sales, B. C.; Mandrus, D.; Williams, R. K. Filled skutterudite antimonides: A new class of thermoelectric materials. *Science* **1996**, *272*, 1325–1328.
- (4) Heremans, J. P.; Jovovic, V.; Toberer, E. S.; Saramat, A.; Kurosaki, K.; Charoenphakdee, A.; Yamanaka, S.; Snyder, G. J. Enhancement of thermoelectric efficiency in PbTe by distortion of the electronic density of states. *Science* **2008**, *321*, 554–557.
- (5) Pei, Y.; Shi, X.; LaLonde, A.; Wang, H.; Chen, L.; Snyder, G. J. Convergence of electronic bands for high performance bulk thermoelectrics. *Nature* **2011**, *473*, 66–69.
- (6) Biswas, K.; He, J.; Blum, I. D.; Wu, C.-I.; Hogan, T. P.; Seidman, D. N.; Dravid, V. P.; Kanatzidis, M. G. High-performance bulk thermoelectrics with all-scale hierarchical architectures. *Nature* **2012**, *489*, 414–418.
- (7) Zhao, L.-D.; Lo, S.-H.; Zhang, Y.; Sun, H.; Tan, G.; Uher, C.; Wolverton, C.; Dravid, V. P.; Kanatzidis, M. G. Ultralow thermal conductivity and high thermoelectric figure of merit in SnSe crystals. *Nature* **2014**, *508*, 373–377.
- (8) Narducci, D. Do we really need high thermoelectric figures of merit? A critical appraisal to the power conversion efficiency of thermoelectric materials. *Appl. Phys. Lett.* **2011**, *99*, 102104.
- (9) Kim, H. S.; Liu, W.; Chen, G.; Chu, C.-W.; Ren, Z. Relationship between thermoelectric figure of merit and energy conversion efficiency. *Proc. Natl. Acad. Sci. U.S.A.* **2015**, *112*, 8205–8210.
- (10) Bartholomé, K.; Balke, B.; Zuckermann, D.; Köhne, M.; Müller, M.; Tarantik, K.; König, J. Thermoelectric Modules Based on Half-

Heusler Materials Produced in Large Quantities. *J. Electron. Mater.* **2013**, *43*, 1775–1781.

(11) Yu, C.; Zhu, T.-J.; Shi, R.-Z.; Zhang, Y.; Zhao, X.-B.; He, J. High-performance half-Heusler thermoelectric materials $\text{Hf}_{1-x}\text{Zr}_x\text{NiSn}_{1-y}\text{Sb}_y$ prepared by levitation melting and spark plasma sintering. *Acta Mater.* **2009**, *57*, 2757–2764.

(12) Joshi, G.; Yan, X.; Wang, H.; Liu, W.; Chen, G.; Ren, Z. Enhancement in Thermoelectric Figure-Of-Merit of an N-Type Half-Heusler Compound by the Nanocomposite Approach. *Adv. Energy Mater.* **2011**, *1*, 643–647.

(13) Chen, L.; Gao, S.; Zeng, X.; Dehkordi, A. M.; Tritt, T. M.; Poon, S. J. Uncovering high thermoelectric figure of merit in $(\text{Hf}/\text{Zr})\text{NiSn}$ half-Heusler alloys. *Appl. Phys. Lett.* **2015**, *107*, 041902.

(14) Gürth, M.; Rogl, G.; Romaka, V. V.; Grytsiv, A.; Bauer, E.; Rogl, P. Thermoelectric high ZT half-Heusler alloys $\text{Ti}_{1-x}\text{Zr}_x\text{Hf}_y\text{NiSn}$ ($0 \leq x \leq 1$; $0 \leq y \leq 1$). *Acta Mater.* **2016**, *104*, 210–222.

(15) Yan, X.; Joshi, G.; Liu, W.; Lan, Y.; Wang, H.; Lee, S.; Simonson, J. W.; Poon, S. J.; Tritt, T. M.; Chen, G.; Ren, Z. F. Enhanced Thermoelectric Figure of Merit of p-Type Half-Heuslers. *Nano Lett.* **2011**, *11*, 556–560.

(16) Fu, C.; Bai, S.; Liu, Y.; Tang, Y.; Chen, L.; Zhao, X.; Zhu, T. Realizing high figure of merit in heavy-band p-type half-Heusler thermoelectric materials. *Nat. Commun.* **2015**, *6*, 8144.

(17) Fu, C.; Zhu, T.; Liu, Y.; Xie, H.; Zhao, X. Band engineering of high performance p-type FeNbSb based half-Heusler thermoelectric materials for figure of merit $zT > 1$. *Energy Environ. Sci.* **2015**, *8*, 216–220.

(18) Rausch, E.; Balke, B.; Stahlhofen, J. M.; Ouardi, S.; Burkhardt, U.; Felser, C. Fine tuning of thermoelectric performance in phase-separated half-Heusler compounds. *J. Mater. Chem. C* **2015**, *3*, 10409–10414.

(19) Bos, J.-W. G.; Downie, R. A. Half-Heusler thermoelectrics: a complex class of materials. *J. Phys.: Condens. Matter* **2014**, *26*, 433201.

(20) Zhu, T.; Fu, C.; Xie, H.; Liu, Y.; Zhao, X. High Efficiency Half-Heusler Thermoelectric Materials for Energy Harvesting. *Adv. Energy Mater.* **2015**, *5*, 1500588.

(21) Makongo, J. P. A.; Misra, D. K.; Zhou, X.; Pant, A.; Shabetai, M. R.; Su, X.; Uher, C.; Stokes, K. L.; Poudeu, P. F. P. Simultaneous Large Enhancements in Thermopower and Electrical Conductivity of Bulk Nanostructured Half-Heusler Alloys. *J. Am. Chem. Soc.* **2011**, *133*, 18843–18852.

(22) Liu, Y.; Sahoo, P.; Makongo, J. P. A.; Zhou, X.; Kim, S.-J.; Chi, H.; Uher, C.; Pan, X.; Poudeu, P. F. P. Large Enhancements of Thermopower and Carrier Mobility in Quantum Dot Engineered Bulk Semiconductors. *J. Am. Chem. Soc.* **2013**, *135*, 7486–7495.

(23) Kirievsky, K.; Gelstein, Y.; Fuks, D. Phase separation and antisite defects in the thermoelectric TiNiSn half-Heusler alloys. *J. Solid State Chem.* **2013**, *203*, 247–254.

(24) Page, A.; Uher, C.; Poudeu, P. F.; Van der Ven, A. Phase separation of full-Heusler nanostructures in half-Heusler thermoelectrics and vibrational properties from first-principles calculations. *Phys. Rev. B: Condens. Matter Mater. Phys.* **2015**, *92*, 174102.

(25) Chai, Y. W.; Kimura, Y. Nanosized precipitates in half-Heusler TiNiSn alloy. *Appl. Phys. Lett.* **2012**, *100*, 033114.

(26) Chai, Y. W.; Kimura, Y. Microstructure evolution of nano-precipitates in half-Heusler TiNiSn alloys. *Acta Mater.* **2013**, *61*, 6684–6697.

(27) Douglas, J. E.; Birkel, C. S.; Miao, M.-S.; Torbet, C. J.; Stucky, G. D.; Pollock, T. M.; Seshadri, R. Enhanced thermoelectric properties of bulk TiNiSn via formation of a TiNi_2Sn second phase. *Appl. Phys. Lett.* **2012**, *101*, 183902.

(28) Birkel, C. S.; Douglas, J. E.; Lettiere, B. R.; Seward, G.; Verma, N.; Zhang, Y.; Pollock, T. M.; Seshadri, R.; Stucky, G. D. Improving the thermoelectric properties of half-Heusler TiNiSn through inclusion of a second full-Heusler phase: microwave preparation and spark plasma sintering of $\text{TiNi}_{1+x}\text{Sn}$. *Phys. Chem. Chem. Phys.* **2013**, *15*, 6990–6997.

(29) Douglas, J. E.; Birkel, C. S.; Verma, N.; Miller, V. M.; Miao, M.-S.; Stucky, G. D.; Pollock, T. M.; Seshadri, R. Phase stability and

property evolution of biphasic Ti-Ni-Sn alloys for use in thermoelectric applications. *J. Appl. Phys.* **2014**, *115*, 043720.

(30) Downie, R. A.; Smith, R. I.; MacLaren, D. A.; Bos, J.-W. G. Metal Distributions, Efficient n-Type Doping, and Evidence for in-Gap States in TiNiM_ySn ($M = \text{Co}, \text{Ni}, \text{Cu}$) half-Heusler Nanocomposites. *Chem. Mater.* **2015**, *27*, 2449–2459.

(31) Larson, A. C.; Von Dreele, R. B. General Structure Analysis System (GSAS). *Los Alamos National Laboratory Report LAUR 86-748*, 2000.

(32) Toby, B. H. EXPGUI, a graphical user interface for GSAS. *J. Appl. Crystallogr.* **2001**, *34*, 210–213.

(33) Xie, H.; Wang, H.; Pei, Y.; Fu, C.; Liu, X.; Snyder, G. J.; Zhao, X.; Zhu, T. Beneficial Contribution of Alloy Disorder to Electron and Phonon Transport in Half-Heusler Thermoelectric Materials. *Adv. Funct. Mater.* **2013**, *23*, 5123–5130.

(34) Downie, R. A.; Barczak, S. A.; Smith, R. I.; Bos, J. W. G. Compositions and thermoelectric properties of XNiSn ($X = \text{Ti}, \text{Zr}, \text{Hf}$) half-Heusler alloys. *J. Mater. Chem. C* **2015**, *3*, 10534–10542.

(35) Xie, H.; Wang, H.; Fu, C.; Liu, Y.; Snyder, G. J.; Zhao, X.; Zhu, T. The intrinsic disorder related alloy scattering in ZrNiSn half-Heusler thermoelectric materials. *Sci. Rep.* **2014**, *4*, 6888.

(36) Kim, H.-S.; Gibbs, Z. M.; Tang, Y.; Wang, H.; Snyder, G. J. Characterization of Lorenz number with Seebeck coefficient measurement. *APL Mater.* **2015**, *3*, 041506.

(37) Eliassen, S. N. H.; Katre, A.; Madsen, G. K. H.; Persson, C.; Løvrik, O. M.; Berland, K. Lattice thermal conductivity of $\text{Ti}_x\text{Zr}_y\text{Hf}_{1-x-y}\text{NiSn}$ half-Heusler alloys calculated from first principles: Key role of nature of phonon modes. *Phys. Rev. B: Condens. Matter Mater. Phys.* **2017**, *95*, 045202.

(38) Uher, C.; Yang, J.; Hu, S.; Morelli, D. T.; Meisner, G. P. Transport properties of pure and doped MNiSn ($M = \text{Zr}, \text{Hf}$). *Phys. Rev. B: Condens. Matter Mater. Phys.* **1999**, *59*, 8615–8621.

(39) Shiomi, J.; Esfarjani, K.; Chen, G. Thermal conductivity of half-Heusler compounds from first-principles calculations. *Phys. Rev. B: Condens. Matter Mater. Phys.* **2011**, *84*, 104302.